www.MaterialsViews.com

Materials
Views

ADVANCED
ENERGY
MATERIALS

www.advenergymat.de

FULL PAPER

Reversible Multivalent (Monovalent, Divalent, Trivalent) Ion Insertion in Open Framework Materials

Richard Y. Wang, Badri Shyam, Kevin H. Stone, Johanna Nelson Weker, Mauro Pasta, Hyun-Wook Lee, Michael F. Toney, and Yi Cui*

The reversible electrochemical insertion of multivalent ions into materials has promising applications in many fields, including batteries, seawater desalination, element purification, and wastewater treatment. However, finding materials that allow for the insertion of multivalent ions with fast kinetics and stable cycling has proven difficult because of strong electrostatic interactions between the highly charged insertion ions and atoms in the host framework. Here, an open framework nanomaterial, copper hexacyanoferrate, in the Prussian Blue family is presented that allows for the reversible insertion of a wide variety of monovalent, divalent, and trivalent ions (such as Rb^+, Pb^{2+}, Al^{3+}, and Y^{3+}) in aqueous solution beyond that achieved in previous studies. Electrochemical measurements demonstrate the unprecedented kinetics of multivalent ion insertion associated with this material. Synchrotron X-ray diffraction experiments point toward a novel vacancy-mediated ion insertion mechanism that reduces electrostatic repulsion and helps to facilitate the observed rapid ion insertion. The results suggest a new approach to multivalent ion insertion that may help to advance the understanding of this complex phenomenon.

1. Introduction

The extraction, exchange, and separation of ions in solution have been studied extensively due to their importance in numerous applications, including seawater desalination[1–3] and delithiation,[4] element purification,[5,6] and wastewater treatment.[7–10] Many of the primary methods for desalination and wastewater treatment employ either filtration membranes[2] or adsorbents[9] that extract a wide variety of ions from solution. Reversible electrochemical insertion of ions into materials would present a valuable alternative to these existing technologies because of the ease of cycling and reuse.

Moreover, the reversible insertion of monovalent ions has been thoroughly explored because of its relevance to intercalation battery electrodes, including electrodes for nickel-metal hydride and lithium-ion batteries.[11,12] The field of multivalent ion intercalation has begun to attract significant research interest recently.[13–15] However, the insertion of divalent or trivalent ions (such as Mg^{2+} or Al^{3+}) into materials has proven difficult; extensive research into magnesium-ion insertion batteries has shown that the additional charge concentration (the ratio of formal charge to ionic radius) on these ions leads to poor insertion kinetics.[16,17]

Prussian Blue (PB) open framework materials have recently demonstrated excellent ion insertion properties,[18–22] including the reversible insertion of divalent alkaline earth ions.[23,24] These properties are primarily a result of the hydrated PB crystal structure. PB analogues possess a well-known perovskite-like face-centered cubic crystal structure in the *Fm*-3*m* space group.[25,26] Extensive crystallography work on PB analogues suggests that carbon–coordinated iron (III/II) and nitrogen–coordinated copper (II) ions reside in the corner sites of the copper hexacyanoferrate (CuHCFe) structure, which correspond to the B sites of the analogous perovskite structure (**Figure 1**a). The cyanide ligands that join iron and copper ions provide structural stability and nanoscale porosity within the crystal structure. Insertion ions reside in and around the interstitial sites,[25–27] which typically correspond to the perovskite A sites (Figure 1a). Within ferricyanide vacancies (Figure 1b), oxygen atoms from water molecules coordinate to the dangling copper ions, and interstitial water molecules reside in and around the A sites.[27–30] Ions inserting into PB analogues likely remain at least partially hydrated,[31] and larger hydrated ions may diffuse through open channels created by these ferricyanide vacancies.[32] Large open A sites (4.6 Å diameter) and ⟨100⟩ channels (3.2 Å diameter) allow for the rapid and reversible insertion of a variety of ions.

The physical and electrochemical properties of PB analogues have been explored thoroughly.[25,26,28,33–42] Electrodeposited thin films of PB exhibit properties that make them useful as
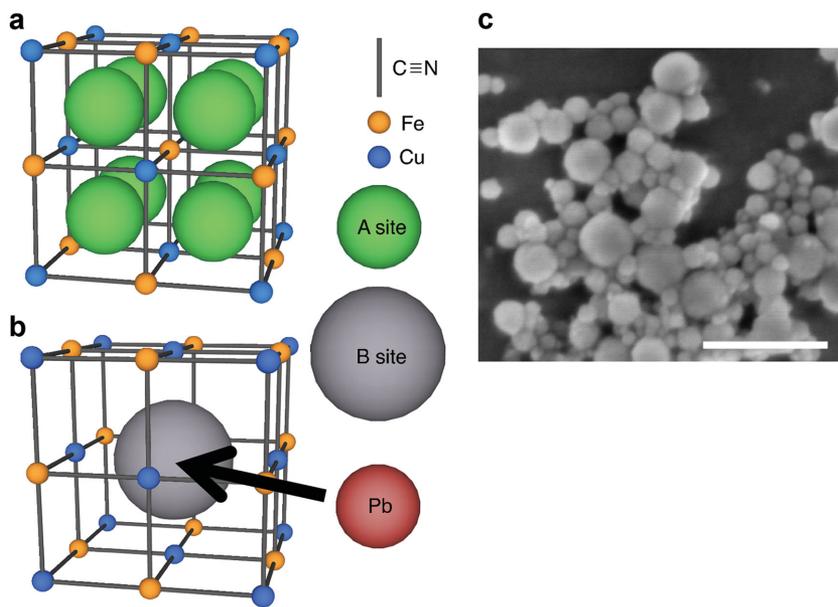
R. Y. Wang, Dr. M. Pasta, Dr. H.-W. Lee, Prof. Y. Cui
Department of Materials Science and Engineering
Stanford University
Stanford, CA 94305, USA
E-mail: yicui@stanford.edu
Dr. B. Shyam, Dr. K. H. Stone, Dr. J. N. Weker,
Dr. M. F. Toney
Stanford Synchrotron Radiation Lightsource
SLAC National Accelerator Laboratory
Menlo Park, CA 94025, USA
Prof. Y. Cui
Stanford Institute for Materials and Energy Sciences
SLAC National Accelerator Laboratory
Menlo Park, CA 94025, USA

FULL PAPER

Figure 1. a) The so-called "soluble" Prussian Blue structure has no vacancies, and insertion ions can only reside in A sites in the center of each cubic sub-cell. The nominal chemical formula in the oxidized state is $KCuFe(CN)_6 * xH_2O$. b) The so-called "insoluble" Prussian Blue structure includes $Fe(CN)_6$ vacancies on ¼ of the iron sites. Water molecules (not shown) coordinated to the copper atoms shield charge, and insertion ions can potentially insert into both A and B sites. The B sites can be thermodynamically favorable for certain insertion ions because coordinated water molecules shield charge from the insertion ion. The nominal chemical formula in the oxidized state is $K_{0.25}Cu(Fe(CN)_6)_{0.75} * xH_2O$. c) The scanning electron image shows polydisperse nanoparticles of CuHCFe ranging from 20 to 90 nm (scale bar = 200 nm).

electrochromic materials.[43–45] PB analogues have shown promise as intercalation battery electrodes in a variety of aqueous and organic electrolytes.[18–22,46–54] While divalent alkaline earth ions have been shown to reversibly insert into nickel hexacyanoferrate with long cycle life and low hysteresis,[23] in this work we demonstrate insertion of a range of divalent transition metal and trivalent rare earth ions in copper hexacyanoferrate with unprecedented kinetics and reversibility that may be facilitated by ferricyanide vacancies. In doing so, we establish successful ion insertion with a much wider range of ions than that achieved in previous studies. Copper hexacyanoferrate serves as a valuable model system for studying the complex phenomenon of multivalent ion insertion.

2. Results and Discussion

2.1. Synthesis

CuHCFe was synthesized by dropwise precipitation of copper nitrate and potassium ferricyanide in aqueous solution following a method previously reported in the literature;[19] specific details can be found in the Methods section. This procedure creates polydisperse nanoparticles of crystalline CuHCFe ranging from 20 to 90 nm in diameter (Figure 1c). The extremely low solubility of Prussian Blue analogues[26] leads to the creation of a high amount of disordered ferricyanide vacancies (usually at least 25%) upon precipitation of the material.[25,26] Elemental analysis and thermogravimetric analysis (TGA) of the CuHCFe

precipitate yields a chemical formula of $K_{0.03}Cu[Fe(CN)_6]_{0.65} \cdot 2.6H_2O$, which suggests that the material is nearly fully oxidized in the as-synthesized state. The partial reduction reflects the tendency of fully oxidized CuHCFe to be reduced in water. Detailed TGA data can be found in Figure S1, Supporting Information.

The maximum theoretical specific capacity is limited by the amount of iron (III) that can be reduced to iron (II) upon ion insertion. The chemical formula predicts a maximum capacity of ≈70 mA h g^{-1} if all iron ions are reduced, but in practice, specific capacities closer to 50 mA h g^{-1} are often observed. As a result, all C rates cited are based on a capacity of 50 mA h g^{-1} (e.g., 1 C = 50 mA g^{-1}). Inconsistency in the ferricyanide vacancy concentration, varying amounts of hydration, and incomplete reduction/oxidation of the material upon insertion/extraction of different ions may contribute to differences in specific capacity across experiments.

2.2. Crystallography

X-ray diffraction (XRD) samples with inserted ions were prepared by electrochemically reducing CuHCFe electrodes with high mass loading (20 mg cm^{-2}) in the presence of 1 M solutions of either rubidium nitrate, lead (II) nitrate, or yttrium nitrate at pH 2. These ions were chosen as model systems because they have high atomic numbers (Z), which increases their sensitivity to X-rays, and because they demonstrate highly reversible electrochemistry. Mechanisms that enable the insertion of multivalent ions would be especially evident in Pb–CuHCFe and Y–CuHCFe because of their electrochemical reversibility. High-resolution synchrotron XRD was performed on powder samples at the Stanford Synchrotron Radiation Laboratory (SSRL) with a wavelength of $\lambda = 1.034$ Å for Rb–CuHCFe and Pb–CuHCFe and with a wavelength of 0.952 Å for Y–CuHCFe. Distinct diffraction peaks can be observed throughout the full Q range of the experiments (**Figure 2**a–c), and all peaks can be indexed with the *Fm*-3*m* space group. The same phase is preserved at different concentrations of insertion ions, as shown in Figure S2, Supporting Information. The cubic lattice parameters for the refined structures are $a_0 = 10.066$, 10.041, and 10.058 Å for Rb–CuHCFe, Pb–CuHCFe, and Y–CuHCFe, respectively. For all three ions, the lattice parameter decreases linearly as ions are inserted (Figure S3, Supporting Information). The relative peak intensities of Rb–CuHCFe and Pb–CuHCFe differ significantly, which reflects differences in site locations and occupancies of ions. Electron microprobe analysis (EMPA) of reduced electrodes (Figure S4, Supporting Information) confirms the electrochemical insertion of multivalent ions.

Rietveld refinement of the XRD data for CuHCFe fully reduced with Rb^+, Pb^{2+}, and Y^{3+} confirms that the *Fm*-3*m* space group accounts for all observed diffraction peaks (Figure 2a,c).

www.MaterialsViews.com

ADVANCED
ENERGY
MATERIALS
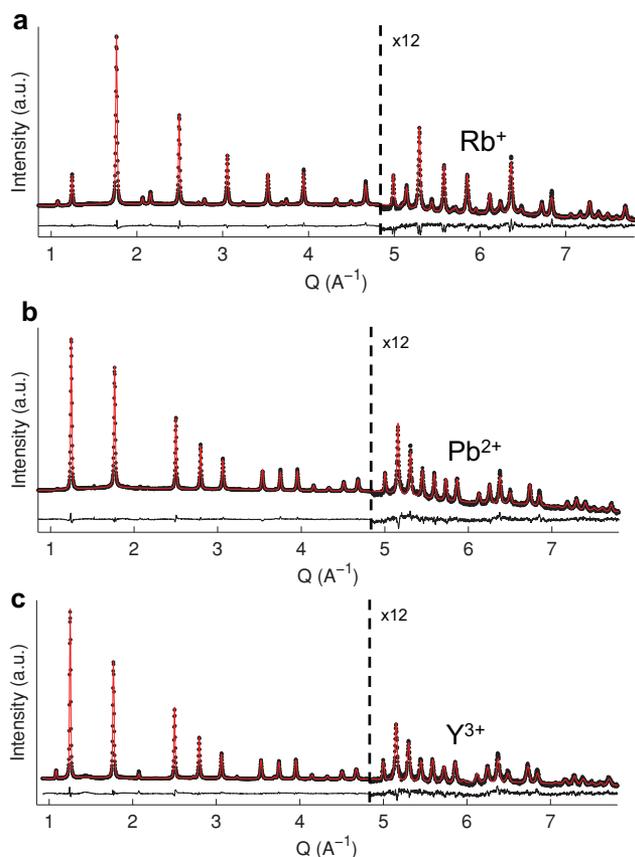www.advenergymat.de

FULL PAPER

Figure 2. Synchrotron X-ray diffractograms (black dots) with Rietveld refinement fits (red line) exhibit different relative peak intensities upon chemical insertion of a) Rb^+, b) Pb^{2+}, and c) Y^{3+} ions. The relatively high X-ray cross-sections of rubidium, lead, and yttrium accentuate the changes in diffraction peaks upon insertion of ions in different sites.

Table 2. The Rietveld refinement for fully reduced CuHCFe with Pb^{2+} inserted shows Pb^{2+} located at both the off-center A (32f) sites and Fe vacancy (4a) sites.

Atom	Site	g	x	y	z	U_{iso}
Fe	4a	0.65	0	0	0	0.035(1)
Pb	4a	0.109(3)	0	0	0	0.035(1)
Cu	4b	1.00	0.5	0.5	0.5	0.038(1)
C	24e	0.65	0.1859(6)	0	0	0.015(1)
N	24e	0.65	0.2862(8)	0	0	0.190(4)
O	24e	0.35	0.2862(8)	0	0	0.190(4)
Pb	32f	0.027	0.2252(3)	0.2252(3)	0.2252(3)	0.130(2)
O	32f	0.042(2)	0.2252(3)	0.2252(3)	0.2252(3)	0.130(2)

same 24e sites, of the iron and insertion ions on the same 4a sites, of the oxygen and insertion ions on the same 8c sites, and of the oxygen and insertion ions on the same 32f sites were constrained to be equal. Figure S5, Supporting Information, presents a schematic of sites within the structure.

Rubidium is included in the model in the iron vacancy 4a sites and the central 8c interstitial sites at (¼, ¼, ¼). Larger monovalent ions (such as Rb) typically reside in these central sites because their ionic size provides geometrical stability within the large interstitial sites in the structure.[55] The Rb occupancy on the 4a sites was freely refined, while the occupancy on the 8c sites was constrained based on the Rb:Cu ratio measured with EMPA (Figure S4, Supporting Information) minus the Rb content refined on the 4a sites. This was necessary because an indeterminate amount of water molecules may share the same interstitial sites as rubidium. The occupancies for oxygen from water molecules were freely refined. The Rb:Cu ratio from EMPA is roughly double that expected based on the measured electrochemical capacity of Rb–CuHCFe, and it may be a result of a partially irreversible insertion of Rb ions into the structure facilitated by a reduction of Cu(II) to Cu(I). Similar behavior (the formation of Cu(I) or irreversibility in CuHCFe) has been observed in some CuHCFe studies,[56–58] but it is not yet clear why only Rb–CuHCFe exhibits this behavior and not Pb–CuHCFe or Y–CuHCFe. Ongoing XANES studies on the chemical states of Fe and Cu in both fully and partially rubidiated CuHCFe may help clarify some of these observations.

Occupancies (g) of iron, carbon, and nitrogen (**Tables 1–3**) are constrained to 0.65 (corresponding to a 35% ferricyanide vacancy content) based on the results of elemental analysis (see above). Water molecules coordinated to the dangling copper ions adjacent to ferricyanide vacancies are represented by oxygen atoms on the 24e sites with a fixed occupancy of 0.35 (all vacant nitrogen sites are filled by oxygen). Positions and thermal parameters of the nitrogen and oxygen atoms on the

Table 1. The Rietveld refinement for fully reduced CuHCFe with Rb^+ inserted shows Rb^+ located primarily at the traditional A (8c) sites.

Atom	Site	g	x	y	z	U_{iso}
Fe	4a	0.65	0	0	0	0.0150(9)
Rb	4a	0.042(4)	0	0	0	0.0150(9)
Cu	4b	1.00	0.5	0.5	0.5	0.0225(5)
Rb	8c	0.574	0.25	0.25	0.25	0.0742(5)
O	8c	0.125(9)	0.25	0.25	0.25	0.0742(5)
C	24e	0.65	0.1809(7)	0	0	0.011(2)
N	24e	0.65	0.2830(5)	0	0	0.132(3)
O	24e	0.35	0.2830(5)	0	0	0.132(3)

Table 3. The Rietveld refinement for fully reduced CuHCFe with Y^{3+} inserted shows Y^{3+} located at both the off-center A (32f) sites and Fe vacancy (4a) sites.

Atom	Site	g	x	y	z	U_{iso}
Fe	4a	0.65	0	0	0	0.028(1)
Y	4a	0.088(4)	0	0	0	0.028(1)
Cu	4b	1.00	0.5	0.5	0.5	0.0330(7)
C	24e	0.65	0.1815(7)	0	0	0.018(2)
N	24e	0.65	0.2902(5)	0	0	0.169(4)
O	24e	0.35	0.2902(5)	0	0	0.169(4)
Y	32f	0.0115	0.222(2)	0.222(2)	0.222(2)	0.06(1)
O	32f	0.232(2)	0.222(2)	0.222(2)	0.222(2)	0.06(1)

Lead and yttrium are included in the model on both the octahedral 4a sites (where the ferricyanide vacancies are located) and on the off-center 32f sites (shared with oxygen from interstitial water molecules). Attempts to refine lead and yttrium on the centered 8c interstitial sites produced fits with high thermal parameters, which correspond to disorder away from the central 8c sites. This off-centering (occupancy on the 32f sites) may be especially prevalent for lead and yttrium because of the high charge concentrations and expected levels of hydration versus those of rubidium (consistent with actual refinement results). The occupancy on the 4a site could be refined without constraints since all other contributions to scattering on the same site are known and fixed. On the other hand, the lead and yttrium occupancy on the 32f sites was fixed based on the amount of lead or yttrium refined in the 4a site subtracted from the total concentration of lead or yttrium determined using EMPA on the same samples (Figure S4, Supporting Information). This 32f occupancy could not be freely refined because an indeterminate amount of oxygen from interstitial water molecules also shares the same site. Refinement statistics for Rb–CuHCFe (R_{wp} = 4.1%, χ^2 = 7.7), Pb–CuHCFe (R_{wp} = 3.0%, χ^2 = 8.4), and Y–CuHCFe (R_{wp} = 5.2%, χ^2 = 4.7) indicate strong agreement between the observed data and the Rietveld model. The residuals of the fits confirm that the large χ^2 values are a result of high counting statistics and not poor crystallographic models.[59]

The refined models point to an interesting and novel difference between monovalent Rb^+ and multivalent Pb^{2+} and Y^{3+} ion insertion in CuHCFe. Rubidium ions mostly insert into the central interstitial sites, which is the commonly accepted view of ion insertion in PB analogues.[41,60] However, lead and yttrium ions occupy both off-center interstitial sites (the 32f sites) and the octahedral B sites (4a sites) formed by ferricyanide vacancies. The occupancies of lead and yttrium on the vacancy sites are more than double that of rubidium, and the difference is strikingly greater when considering the fraction of total capacity accommodated by insertion into the vacancy sites (3.5% for Rb–CuHCFe versus 34% and 49% for Pb–CuHCFe and Y–CuHCFe, respectively, after accounting for the differing site multiplicities). The divalent charge on a lead ion and the trivalent charge on an yttrium ion attract larger hydration shells due to the stronger electrostatic interaction between the charged ions and the dipoles of water molecules (compared to the hydration shell of a rubidium ion). The difference in hydration is consistent with the refinement of more oxygen from water molecules in Pb–CuHCFe and Y–CuHCFe than in Rb–CuHCFe. As a result, hydrated lead and yttrium ions have a larger effective radius than hydrated rubidium ions, even though unhydrated lead and yttrium ions have a smaller ionic radius than unhydrated rubidium ions.[61,62]

Lead and yttrium ions may occupy the iron vacancy sites within CuHCFe because the larger size of these sites allows lead and yttrium to be either more hydrated or adjacent to more coordinated water molecules within the structure than they would otherwise be in an interstitial site. The larger hydration shell would provide a greater thermodynamic stability for lead and yttrium ions in the vacancy sites than for rubidium ions due to the extra shielding of the multivalent charges on lead and yttrium. Such a mechanism would allow lead and yttrium ions to reside in vacancy sites that would otherwise be thermodynamically

unfavorable relative to the interstitial sites. The vacancy sites are too large for bare ions to reside in easily. Further, we note that this shielding mechanism is similar to that postulated for the charge shielding observed in magnesium-ion battery electrodes[17] and suggests that such screening/shielding effects may be more prominent in many multivalent ions, which is consistent with chemical intuition.

2.3. Electrochemistry

We have previously reported on novel electrochemistry for reversible insertion of divalent alkaline earth ions in nickel hexacyanoferrate.[23] In our present experiments, we have expanded upon that work, and we can now report insertion of a wide variety of divalent and trivalent ions from the transition metal and rare earth families in copper hexacyanoferrate with unprecedented electrochemical performance. We further show how the structural details of ion insertion into copper hexacyanoferrate described above provide an understanding of aspects of the electrochemical performance.

Cyclic voltammograms (CVs) demonstrate reversible insertion of many different divalent ions in CuHCFe (**Figure 3**a,b). Both the insertion voltages and the qualitative shapes of the CVs vary significantly as a function of the insertion ion. The presence of multiple cathodic and anodic peaks at different voltages in the data suggests that there are multiple electrochemical processes at work during divalent ion insertion. Our Rietveld refinement of high-resolution XRD data has conclusively demonstrated insertion of Pb^{2+} and Y^{3+} ions in both A and B sites in the structure, and it appears that the multiple CV peaks correspond to divalent ions inserting into these electrochemically distinct sites in the structure, although in situ XRD is required to demonstrate this conclusively. Conversely, the insertion of Rb^+ in Prussian Blue analogues exhibits one distinct CV peak (Figure S6, Supporting Information)[40] which is typical for insertion of alkali ions in these materials and also consistent with refinement results of crystallographic data.

Galvanostatic cycling at 5 C (corresponding to a 12 min charge or discharge) reflects the rapid kinetics associated with inserting divalent ions into CuHCFe (Figure 3c). The characteristic S-shaped sloping potential profile reflects the single-phase insertion reaction for all ions in CuHCFe. More than 50% of the specific capacity observed at C/5 is retained when cycling these divalent ions at 5 C; detailed data on the rate dependence of each insertion ion can be found in Figures S7 and S8, Supporting Information. The voltage hysteresis at half charge for a 5 C cycling rate ranges from 50 mV for Ni^{2+} to 141 mV for Co^{2+}, which is remarkably low for divalent ion insertion. Water molecules provide charge shielding that allows for efficient diffusion of divalent ions, and the observation is consistent with the higher levels of hydration seen in our Rietveld refinements in Pb–CuHCFe and Y–CuHCFe versus that of Rb–CuHCFe. In comparison, the voltage hysteresis is usually at least 300 mV for Mg^{2+} insertion at rates below C/5 in many magnesium-ion battery cathodes (V_2O_5, MnO_2, $MnSiO_4$, and others).[17,63,64] This is not a direct comparison of material properties since most of these magnesium-ion electrode studies are performed in organic electrolyte, which also contributes to poor kinetics
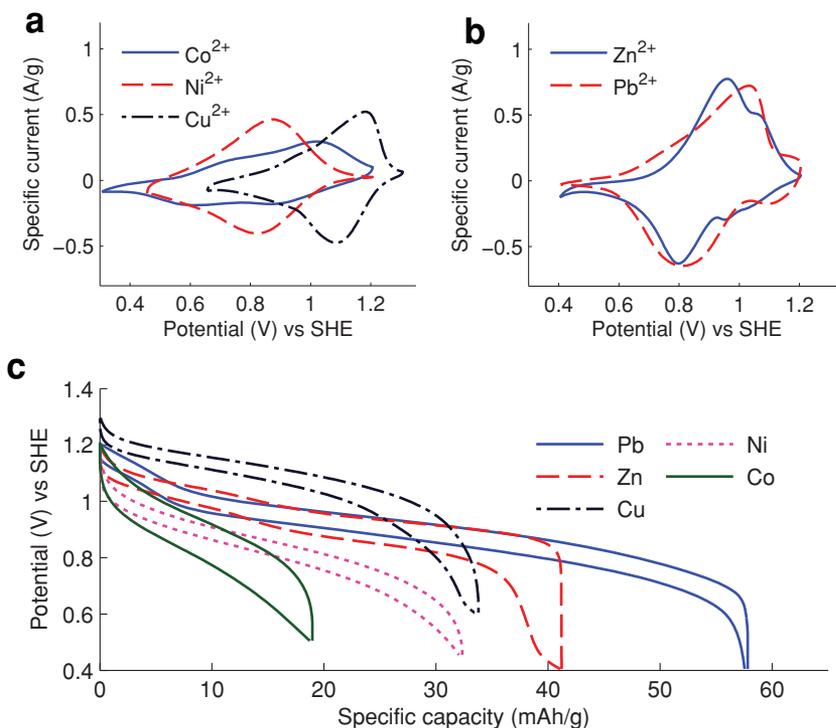
Figure 3. a,b) Cyclic voltammograms (1 mV s^{-1} sweep rate) demonstrate reversible insertion of a variety of divalent ions in CuHCFe. c) Galvanostatic cycling of divalent ions in CuHCFe at 5 C shows low voltage hysteresis and retention of specific capacity even at a high charge/discharge rate.

of ionic diffusion. Nevertheless, both the specific capacity retention and low voltage hysteresis demonstrate the excellent kinetics of divalent ion insertion in CuHCFe.

The size of CuHCFe crystallites (Figure S9, Supporting Information) should not have a noticeable impact on the rates of ion insertion because of the rapid diffusion of ions within the crystal. In fact, the diffusion constants of ions within nickel hexacyanoferrate, a closely related Prussian Blue analogue, are almost as high as those in aqueous solutions.[65] Moreover, other Prussian Blue analogues with crystallite sizes up to 500 nm have demonstrated rapid ion insertion,[21] so the CuHCFe morphology should not have a significant impact on its kinetics.

Extended galvanostatic cycling of divalent ions at 5 C over 2000 cycles demonstrates the high structural integrity of CuHCFe (**Figure 4**a–d) even after such extended cycling. In the case of Ni^{2+} and Zn^{2+}, there is a large initial drop in capacity before the capacity decay stabilizes, which suggests difficulty in reversibly inserting these ions into all available sites in the structure. There is no evidence to suggest a change in crystal structure or decrease in crystallinity after cycling. One possible explanation for the capacity fade may involve swapping of insertion ions with framework metal ions, which has previously been observed in CuHCFe.[57] The partially transformed Prussian Blue analogue may not be as electrochemically active as CuHCFe, which could account for the capacity fade. However, the morphology and structure would remain nearly unchanged after this happened, so it is difficult to isolate the mechanism of the capacity fade conclusively.

Cu^{2+} and Pb^{2+} do not exhibit this initial capacity decay, which is why they retain much more of their initial capacity after 2000 cycles. In the case of Cu^{2+} in CuHCFe, the insertion voltage shows a strong temperature dependence (consistent with past work),[66] and the daily fluctuations in ambient temperature in the lab lead to the fluctuations in capacity in the cycling data. The Cu^{2+} insertion voltage is almost 200 mV higher than the insertion voltages of the other divalent ions (Figure 3), which means that inserting Cu^{2+} in the structure is more thermodynamically favorable. These electrochemical properties, which are unique to Cu^{2+} insertion in CuHCFe, may indicate that insertion ions are directly interacting with the copper ions on the B sites in the framework. However, the current understanding of ion insertion in PB analogues[31,32,41,42,67] provides no comprehensive explanation for why electrochemical properties vary so significantly with the choice of insertion ion. The Rietveld refinement results presented above suggest that vacancies and water molecules may facilitate ion insertion, but the detailed mechanism of ion insertion in PB analogues remains a topic of ongoing study.

The average coulombic efficiency (Figure 4a–d) stays above 99% for all the divalent insertion ions, which reflects slow side reactions and a remarkably high chemical stability of the electrodes and electrolytes during high-rate cycling. The overall energy efficiency of the full cell, calculated versus an activated carbon negative electrode, is very stable and remains above 80% for Cu^{2+}, Zn^{2+}, and Pb^{2+}. This is a result of the low voltage hysteresis for divalent ion insertion, which does not change appreciably over 2000 cycles. The energy efficiency for Ni^{2+} insertion starts below 80% and decreases further, which correlates with the rapid drop in specific capacity with cycling and suggests difficulty in reversibly inserting Ni^{2+}.

All of the physical and structural properties that make CuHCFe ideal for monovalent and divalent ion insertion enable the reversible electrochemical insertion of a wide variety of trivalent insertion ions as well, which has never before been observed in any material. Cyclic voltammograms demonstrate reversible insertion of six different trivalent ions, most of which come from the rare earth series of elements (**Figure 5**a,b). The shapes of the voltammograms are generally more poorly defined than those of monovalent and divalent ion insertion, and trivalent ions appear to insert gradually over a wider range of voltages. Each voltammogram exhibits multiple cathodic and anodic peaks separated by 100 to 300 mV, which suggests a complex insertion mechanism with more thermodynamically distinct insertion sites for each ion. This may correspond to variations in the level of dehydration required for ions to be inserted into different sites within the structure. The refinement results suggest much greater levels of hydration in Y–CuHCFe than in Rb–CuHCFe or Pb–CuHCFe, which is consistent with
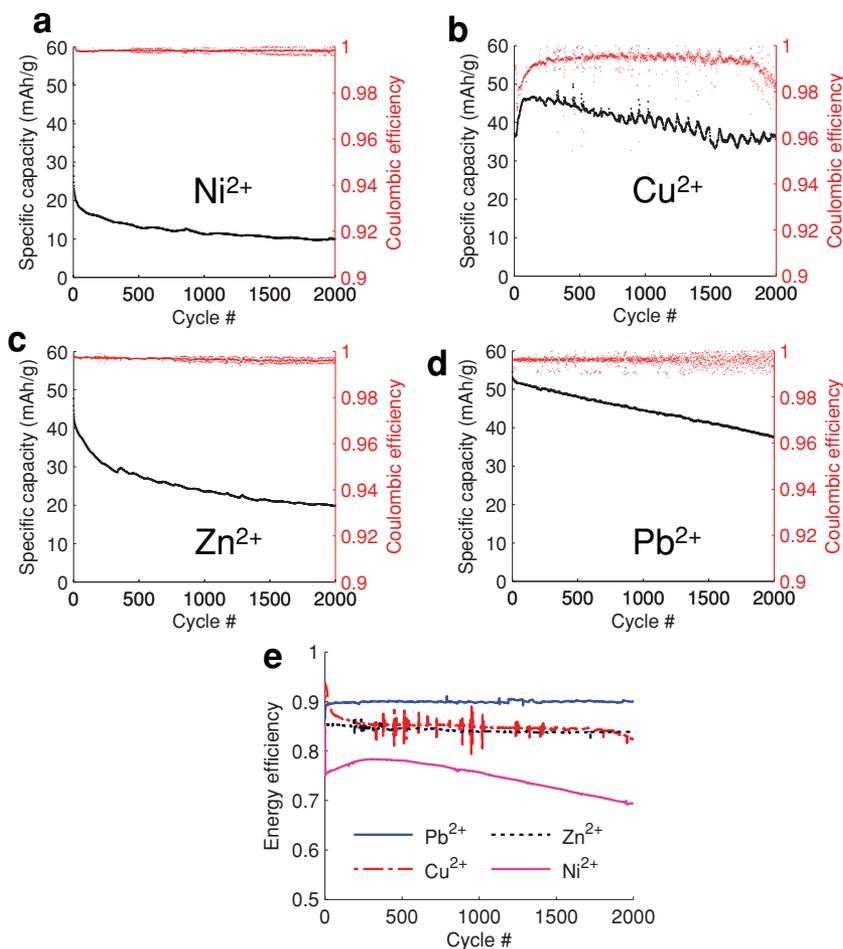
Figure 4. Retention of specific capacity and coulombic efficiency over 2000 cycles at 5 C for a) Ni^{2+}, b) Cu^{2+}, c) Zn^{2+}, and d) Pb^{2+} reflects the stability of the material during insertion/extraction of multivalent ions. e) Energy efficiency versus activated carbon negative electrodes remains above 80% after 2000 cycles for all ions except nickel and illustrates retention of low voltage hysteresis after extended cycling.

trivalent ions, respectively, that were studied. Increasing the galvanostatic cycling rate by a factor of 50, from C/5 to 10 C, decreases the specific capacity by less than 15% for all of these ions (Figure 5e–g). The voltage hysteresis remains at less than 120 mV at 10 C, even with complete insertion or extraction of the ions in only 6 min. In the most optimal cases, increasing the oxidation state of the insertion ion from +1 to +2 or +3 has a negligible impact on insertion chemistry in CuHCFe (performance is consistent with a previous study of Mg^{2+} insertion in CuHCFe),[24] which is counterintuitive since the charge state is usually the strongest determining factor of electrochemical insertion in other materials. Taken together, these observations suggest a high degree of charge screening, likely from water molecules in the hydration shell or in the structure (consistent with the refinement results), which minimizes the electrostatic interaction between the insertion ion and the host ions that make up CuHCFe.

The unhydrated crystal ionic radii of the multivalent insertion ions in octahedral geometry[62] range from 0.675 Å for Al^{3+} to 1.33 Å for Pb^{2+} (**Table 4**). In all cases, the radii are smaller than the 1.6 Å channel radius in CuHCFe, so if the ions are not hydrated, all of these ions should be able to diffuse through the ⟨100⟩ channels. However, these ions are most likely at least partially hydrated since there appears to be a high degree of charge screening that enables the rapid insertion kinetics of divalent and trivalent ions. This is supported by the Rietveld refinement results, which suggest that divalent and trivalent ions require additional hydration to remain in the structure. It is unclear if hydrated insertion ions are diffusing through alternative pathways, such as the proposed ferricyanide vacancy pathway,[32,67] if ions are hydrated only along the ⟨100⟩ axes during diffusion,[39] or if both mechanisms contribute to ionic diffusion in CuHCFe.

The insertion voltage for these multivalent ions varies widely, from 0.76 V versus SHE for Al^{3+} to 1.13 V versus SHE for Cu^{2+} (Table 4). A graphical comparison of the ion insertion voltages can be found in Figure S10, Supporting Information. The ion insertion voltage is determined by the change in free energy of hydration of the ion upon insertion and the change in free energy due to the changing bonding environment upon insertion.[39,42] The free energy of hydration correlates with the insertion voltage for monovalent ions,[42] but the trend does not hold for divalent or trivalent ions. In addition, many of the multivalent ion CVs exhibit multiple cathodic and anodic peaks at distinct voltages, which is consistent with ions inserting into multiple distinct crystallographic sites (consistent with the structural results) or undergoing different degrees of dehydration during insertion.[39] The variations in insertion voltage and
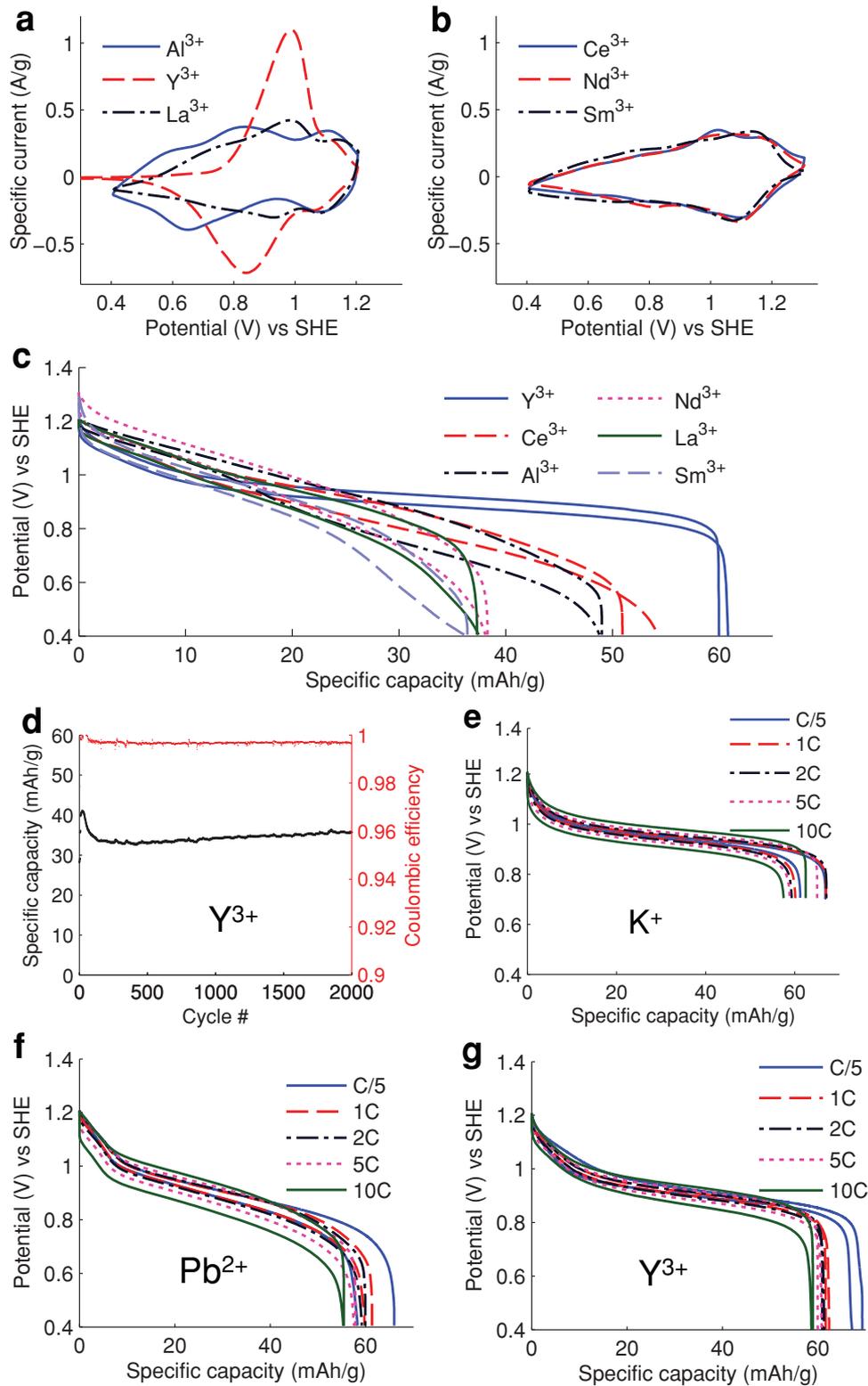
this observation. The CVs of Ce^{3+}, Nd^{3+}, and Sm^{3+} are strikingly similar (Figure 5b), which reflects the chemical similarity of many of the rare earth elements.

Galvanostatic cycling of trivalent ions at 5 C demonstrates the rapid kinetics of trivalent ion insertion in CuHCFe (Figure 5c). Over 60% of the specific capacity observed at C/5 is retained when cycling these trivalent ions at 5 C; detailed data on the rate dependence of each insertion ion can be found in Figure S6–S8, Supporting Information. The voltage hysteresis at half charge for a 5 C cycling rate ranges from 36 mV for Y^{3+} to 124 mV for Al^{3+}, which is remarkably low for trivalent ion insertion and even lower than the hysteresis observed for divalent ion insertion. This may be enabled by the especially high level of hydration in Y–CuHCFe confirmed by the refinement results. Extended cycling of Y^{3+} at 5 C demonstrates structural stability over time, which results in retention of specific capacity with cycling and coulombic efficiency over 99.5% (Figure 5d).

CuHCFe exhibits extremely rapid kinetics for multivalent ion insertion. K^+, Pb^{2+}, and Y^{3+} exhibit the fastest and most reversible electrochemistry out of the monovalent, divalent, and

www.MaterialsViews.com

ADVANCED
ENERGY
MATERIALS
www.advenergymat.de

FULL PAPER

Figure 5. a,b) Cyclic voltammograms demonstrate reversible insertion of a variety of trivalent ions in CuHCFe. c) Galvanostatic cycling of trivalent ions in CuHCFe at 5 C shows low voltage hysteresis and retention of specific capacity even at high charge/discharge rates. d) Stable cycling of Y^{3+} over 2000 cycles with high coulombic efficiency reflects the ease of insertion of highly charged ions in CuHCFe. The initial capacity may be lower than that in the galvanostatic experiments because of difficulty in consistently determining the mass of each electrode. Galvanostatic cycling experiments of e) K^+, f) Pb^{2+}, and g) Y^{3+} in CuHCFe demonstrate that increasing the charge of insertion ions does not necessarily lead to worsened kinetics.

FULL PAPER

Table 4. The crystal ionic radii[62] of these insertion ions with octahedral coordination are all smaller than the theoretical radius of 1.6 Å for the 100⟩ diffusion channels in CuHCFe.[36] The insertion voltages of insertion ions in CuHCFe vary widely, from 0.76 to 1.13 V versus SHE. The voltages are calculated by taking the mean of the voltages corresponding to peak cathodic and anodic currents during cyclic voltammetry.

Ion	Ionic radii [Å]	Voltage [V] versus SHE
Co^{2+}	0.885	0.84
Ni^{2+}	0.83	0.85
Cu^{2+}	0.87	1.13
Zn^{2+}	0.88	0.88
Pb^{2+}	1.33	0.91
Al^{3+}	0.675	0.76
Y^{3+}	1.04	0.91
La^{3+}	1.172	0.96
Ce^{3+}	1.15	1.04
Nd^{3+}	1.123	1.02
Sm^{3+}	1.098	1.08

kinetics of different multivalent ions reflect the complex mechanisms at work during multivalent ion insertion, and these mechanisms remain a topic of ongoing study.

3. Conclusion

CuHCFe nanoparticles can be synthesized by dropwise addition of precursors in aqueous solution at room temperature. The material is cubic and highly crystalline yet contains a significant concentration of ferricyanide vacancies that play an essential role in ion insertion. Rietveld refinement of synchrotron X-ray diffraction data shows that Rb^+, Pb^{2+}, and Y^{3+} insert into different sites in the crystal structure, which suggests that ions can insert into CuHCFe through multiple pathways. Electrochemical cycling demonstrates the reversible and unprecedented insertion of both divalent transition metal and trivalent rare earth ions into CuHCFe with high rates and low hysteresis.

Our experimental results suggest that the presence of ferricyanide vacancies and water molecules in the structure both play significant roles in allowing for the reversible insertion of multivalent ions. The insertion of Pb^{2+} and Y^{3+} into ferricyanide vacancies, along with previous work on the role of vacancies as a cation diffusion path,[32] suggest that vacancies help to enable insertion of multivalent ions. Vacancies can also redistribute concentrated charge in the structure[68] and stabilize the cubic PB phase.[69] Water molecules and partially hydrated insertion ions in the structure can reduce the activation energy for interfacial charge transfer during insertion[31] and assist ionic diffusion through the material.[67] These features provide PB materials with their remarkable electrochemical properties.

Preparing CuHCFe samples with varying vacancy contents and measuring their electrochemical properties would help to confirm the role of vacancies in facilitating multivalent ion insertion. Unfortunately, synthesizing low-vacancy CuHCFe is challenging because of its low solubility and rapid precipitation and crystallization from solution. Adapting existing methods for synthesizing low-vacancy Prussian Blue analogues[22] may produce more encouraging results.

The reversible insertion of a wide variety of multivalent ions into copper hexacyanoferrate may have potential applications in multivalent batteries (such as Mg- and Al-ion batteries), seawater desalination and delithiation, elemental purification, and wastewater treatment. Furthermore, the present work provides fundamental insight into the mechanism by which multivalent ions insert into PB materials. A more complete understanding of multivalent ion insertion may help guide the design of new materials with improved electrochemical properties, which have many applications in energy storage and environmental cleanup.

Much remains unknown about the ion insertion mechanism in PB analogues, including the extent and specific role of ion hydration, the variation of electrochemical properties with ionic properties, and the mechanisms of charge transfer within the structure upon ion insertion. Ongoing studies with synchrotron X-ray diffraction, X-ray absorption spectroscopy, low-temperature neutron diffraction, solid-state NMR, and cycling of PB analogues in aqueous and organic electrolytes can help to answer some of these remaining questions.

4. Experimental Section

CuHCFe Synthesis: CuHCFe nanoparticles were prepared based on our previously reported synthesis procedure.[19] Equal amounts of $Cu(NO_3)_2$ (40×10^{-3} M, Alfa Aesar) and $K_3Fe(CN)_6$ (20×10^{-3} M, Sigma-Aldrich) were combined by dropwise addition into deionized water and stirred for 1 h. After allowing the precipitate to settle overnight, excess water was decanted from the mixture. The powder was isolated from solution by vacuum filtration, washed with water, and dried in vacuum at room temperature.

Electrode Fabrication: A slurry of CuHCFe was prepared by grinding together 80% w/w CuHCFe, 10% w/w polyvinylidene fluoride (Kynar), and 10% w/w Super P Li (Timcal) and adding 1-methyl-2-pyrrolidinone (Sigma-Aldrich) until a thick and smooth slurry was formed. The slurry was applied onto carbon cloth (Fuel Cell Earth) with a mass loading of approximately 10 mg cm^{-2} and dried under vacuum at 80 °C.

Activated carbon counter electrodes were prepared by grinding together 80% w/w activated carbon (Sigma-Aldrich) and 20% w/w polyvinylidene fluoride (Kynar) and adding 1-methyl-2-pyrrolidinone (Sigma-Aldrich) until a smooth slurry was formed. The slurry was applied onto carbon cloth (Fuel Cell Earth) with a mass loading of approximately 50–100 mg cm^{-2} and dried under vacuum at 80 °C.

Electrochemical Experiments: Electrochemical measurements were performed in a three-electrode flooded half cell configuration with a CuHCFe working electrode, a silver/silver chloride (4 M KCl) reference electrode (Fisher Scientific), and either a platinum (Fisher Scientific) or activated carbon counter electrode. Electrolytes were prepared by dissolving nitrate salts in deionized water to a 1 M concentration and adding nitric acid to maintain a pH of 2. All C rates assume a maximum specific capacity of 50 mA h g^{-1} of CuHCFe.

X-Ray Diffraction: CuHCFe electrodes with approximately 20 mg cm^{-2} mass loading were cycled five times in $RbNO_3$, $Pb(NO_3)_2$, or $Y(NO_3)_3$ (1 M, pH 2) at 1 C to determine the capacity of each electrode, then they were reduced or oxidized to the desired state of charge at a 1 C rate. X-ray diffraction data were collected on beamline 2–1 at the Stanford Synchrotron Radiation Lightsource (SSRL) at SLAC National Accelerator Laboratory. Experiments were run at room temperature with a step size of 0.02° in 2θ with a wavelength of $\lambda = 1.034$ (for Rb–CuHCFe and Pb–CuHCFe) or 0.952 Å (for Y–CuHCFe) with a monochromator and Soller slits in a Bragg–Brentano geometry. Backgrounds in the data were fitted

www.MaterialsViews.com

ADVANCED
ENERGY
MATERIALS
www.advenergymat.de

FULL PAPER

with multiterm shifted Chebyshev polynomial functions. All thermal parameters (U_{iso}) were refined isotropically. Reported occupancies (g) reflect the proportion of equivalent crystallographic sites occupied by each ion and do not account for the differing multiplicities of each site. Refined unit cells contain $Z = 4$ formula units. Rietveld refinements were done with the EXPGUI interface for GSAS.[70,71]

Supporting Information

Supporting Information is available from the Wiley Online Library or from the author.

Acknowledgements

[1] Y. Oren, *Desalination* **2008**, *228*, 10.

[2] M. Elimelech, W. A. Phillip, *Science* **2011**, *333*, 712.

[3] M. Pasta, C. D. Wessells, Y. Cui, F. La Mantia, *Nano Lett.* **2012**, *12*, 839.

[4] M. Pasta, A. Battistel, F. La Mantia, *Energy Environ. Sci.* **2012**, *5*, 9487.

[5] B. Ketelle, G. Boyd, *J. Am. Chem. Soc.* **1947**, *69*, 2800.

[6] E. R. Tompkins, S. W. Mayer, *J. Am. Chem. Soc.* **1947**, *69*, 2859.

[7] G. E. Boyd, A. W. Adamson, L. S. Myers Jr., *J. Am. Chem. Soc.* **1947**, *69*, 2836.

[8] L. Ćurković, Š. Cerjan-Stefanović, T. Filipan, *Water Res.* **1997**, *31*, 1379.

[9] S. Babel, T. A. Kurniawan, *J. Hazard. Mater.* **2003**, *97*, 219.

[10] G. Chen, *Sep. Purif. Technol.* **2004**, *38*, 11.

[11] J. Willems, *J. Philips J. Res.* **1984**, *39*, 1.

[12] K. Mizushima, P. C. Jones, P. J. Wiseman, J. B. Goodenough, *Mater. Res. Bull.* **1980**, *15*, 783.

[13] J. Muldoon, C. B. Bucur, T. Gregory, *Chem. Rev.* **2014**, *114*, 11683.

[14] M. R. Lukatskaya, O. Mashtalir, C. E. Ren, Y. Dall'Agnese, P. Rozier, P. L. Taberna, M. Naguib, P. Simon, M. W. Barsoum, Y. Gogotsi, *Science* **2013**, *341*, 1502.

[15] M. Liu, Z. Rong, R. Malik, P. Canepa, A. Jain, G. Ceder, K. Persson, *Energy Environ. Sci.* **2015**, *8*, 964.

[16] D. Aurbach, G. S. Suresh, E. Levi, A. Mitelman, O. Mizrahi, O. Chusid, M. Brunelli, *Adv. Mater.* **2007**, *19*, 4260.

[17] E. Levi, Y. Gofer, D. Aurbach, *Chem. Mater.* **2010**, *22*, 860.

[18] C. D. Wessells, S. V. Peddada, R. A. Huggins, Y. Cui, *Nano Lett.* **2011**, *11*, 5421.

[19] C. D. Wessells, R. A. Huggins, Y. Cui, *Nat. Commun.* **2011**, *2*, 550.

[20] M. Pasta, C. D. Wessells, R. A. Huggins, Y. Cui, *Nat. Commun.* **2012**, *3*, 1149.

[21] M. Pasta, C. D. Wessells, N. Liu, J. Nelson, M. T. McDowell, R. A. Huggins, M. F. Toney, Y. Cui, *Nat. Commun.* **2014**, *5*, 3007.

[22] H.-W. Lee, R. Y. Wang, M. Pasta, S. Woo Lee, N. Liu, Y. Cui, *Nat. Commun.* **2014**, *5*, 5280.

[23] R. Y. Wang, C. D. Wessells, R. A. Huggins, Y. Cui, *Nano Lett.* **2013**, *13*, 5748.

[24] Y. Mizuno, M. Okubo, E. Hosono, T. Kudo, K. Oh-ishi, A. Okazawa, N. Kojima, R. Kurono, S. Nishimura, A. Yamada, *J. Mater. Chem. A* **2013**, *1*, 13055.

[25] A. Ludi, H. Güdel, *Inorg. Chem.* **1973**, *14*, 1.

[26] H. J. Buser, D. Schwarzenbach, W. Petter, A. Ludi, *Inorg. Chem.* **1977**, *16*, 2704.

[27] Y. Moritomo, T. Matsuda, Y. Kurihara, J. Kim, *J. Phys. Soc. Jpn.* **2011**, *80*, 074608.

[28] F. Herren, P. Fischer, A. Ludi, W. Hälg, *Inorg. Chem.* **1980**, *19*, 956.

[29] P. R. Bueno, F. F. Ferreira, D. Giménez-Romero, G. Oliveira Setti, R. C. Faria, C. Gabrielli, H. Perrot, J. J. Garcia-Jareño, F. Vicente, *J. Phys. Chem. C* **2008**, *112*, 13264.

[30] P. Bhatt, N. Thakur, M. D. Mukadam, S. S. Meena, S. M. Yusuf, *J. Phys. Chem. C* **2013**, *117*, 2676.

[31] Y. Mizuno, M. Okubo, E. Hosono, T. Kudo, H. Zhou, K. Oh-ishi, *J. Phys. Chem. C* **2013**, *117*, 10877.

[32] Y. Moritomo, K. Igarashi, J. Kim, H. Tanaka, *Appl. Phys. Express* **2009**, *2*, 085001.

[33] J. F. Keggin, F. D. Miles, *Nature* **1936**, *137*, 577.

[34] G. W. Beall, W. O. Milligan, J. Korp, I. Bernal, *Inorg. Chem.* **1977**, *16*, 2715.

[35] V. D. Neff, *J. Electrochem. Soc.* **1978**, *125*, 886.

[36] K. Itaya, T. Ataka, S. Toshima, *J. Am. Chem. Soc.* **1982**, *104*, 4767.

[37] K. Itaya, I. Uchida, V. D. Neff, *Acc. Chem. Res.* **1986**, *19*, 162.

[38] J. W. McCargar, V. D. Neff, *J. Phys. Chem.* **1988**, *92*, 3598.

[39] F. Scholz, A. Dostal, *Angew. Chem. Int. Ed.* **1996**, *34*, 2685.

[40] A. Dostal, G. Kauschka, S. J. Reddy, F. Scholz, *J. Electroanal. Chem.* **1996**, *406*, 155.

[41] A. Widmann, H. Kahlert, I. Petrovic-Prelevic, H. Wulff, J. V. Yakhmi, N. Bagkar, F. Scholz, *Inorg. Chem.* **2002**, *41*, 5706.

[42] M. Bárcena Soto, F. Scholz, *J. Electroanal. Chem.* **2002**, *521*, 183.

[43] D. Ellis, M. Eckhoff, V. D. Neff, *J. Phys. Chem.* **1981**, *85*, 1225.

[44] K. P. Rajan, V. D. Neff, *J. Phys. Chem.* **1982**, *86*, 4361.

[45] K. Itaya, K. Shibayama, H. Akahoshi, S. Toshima, *J. Appl. Phys.* **1982**, *53*, 804.

[46] C. D. Wessells, M. T. McDowell, S. V. Peddada, M. Pasta, R. A. Huggins, Y. Cui, *ACS Nano* **2012**, *6*, 1688.

[47] C. D. Wessells, S. V. Peddada, M. T. McDowell, R. A. Huggins, Y. Cui, *J. Electrochem. Soc.* **2012**, *159*, A98.

[48] T. Matsuda, Y. Moritomo, *Appl. Phys. Express* **2011**, *4*, 047101.

[49] D. Asakura, M. Okubo, Y. Mizuno, T. Kudo, H. Zhou, K. Ikedo, T. Mizokawa, A. Okazawa, N. Kojima, *J. Phys. Chem. C* **2012**, *116*, 8364.

[50] Y. Moritomo, M. Takachi, Y. Kurihara, T. Matsuda, *Appl. Phys. Express* **2012**, *5*, 041801.

[51] H. Lee, Y.-I. Kim, J.-K. Park, J. W. Choi, *Chem. Commun.* **2012**, *48*, 8416.

[52] Y. Lu, L. Wang, J. Cheng, J. B. Goodenough, *Chem. Commun.* **2012**, *48*, 6544.

[53] T. Matsuda, M. Takachi, Y. Moritomo, *Chem. Commun.* **2013**, 3.

[54] L. Wang, Y. Lu, J. Liu, M. Xu, J. Cheng, D. Zhang, J. B. Goodenough, *Angew. Chem. Int. Ed.* **2013**, *52*, 1964.

[55] E. J. M. Vertelman, E. Maccallini, D. Gournis, P. Rudolf, T. Bakas, J. Luzon, R. Broer, A. Pugzlys, T. T. A. Lummen, P. H. M. van Loosdrecht, P. J. van Koningsbruggen, *Chem. Mater.* **2006**, *18*, 1951.

[56] O. Makowski, J. Stroka, P. J. Kulesza, M. A. Malik, Z. Galus, *J. Electroanal. Chem.* **2002**, *532*, 157.

FULL PAPER

[57] M. Giorgetti, L. Guadagnini, D. Tonelli, M. Minicucci, G. Aquilanti, *Phys. Chem. Chem. Phys.* **2012**, *14*, 5527.

[58] S. Ayrault, B. Jimenez, E. Garnier, M. Fedoroff, D. J. Jones, *J. Solid State Chem.* **1998**, *485*, 475.

[59] B. H. Toby, *Powder Diffr.* **2006**, *21*, 67.

[60] C. Ling, J. Chen, F. Mizuno, *J. Phys. Chem. C* **2013**, *117*, 21158.

[61] E. R. Nightingale, *J. Phys. Chem.* **1959**, *63*, 1381.

[62] R. D. Shannon, *Acta Crystallogr. Sect. A* **1976**, *32*, 751.

[63] Y. NuLi, J. Yang, J. Wang, Y. Li, *J. Phys. Chem. C* **2009**, *113*, 12594.

[64] R. Zhang, X. Yu, K.-W. Nam, C. Ling, T. S. Arthur, W. Song, A. M. Knapp, S. N. Ehrlich, X.-Q. Yang, M. Matsui, *Electrochem. Commun.* **2012**, *23*, 110.

[65] H.-W. Lee, M. Pasta, R. Y. Wang, R. Ruffo, Y. Cui, *Faraday Discuss.* **2014**, *176*, 69.

[66] S. W. Lee, Y. Yang, H.-W. Lee, H. Ghasemi, D. Kraemer, G. Chen, Y. Cui, *Nat. Commun.* **2014**, *5*, 3942.

[67] S.-I. Ohkoshi, K. Nakagawa, K. Tomono, K. Imoto, Y. Tsunobuchi, H. Tokoro, *J. Am. Chem. Soc.* **2010**, *132*, 6620.

[68] A. Flambard, F. H. Köhler, R. Lescouëzec, *Angew. Chem. Int. Ed.* **2009**, *121*, 1701.

[69] Y. Kurihara, T. Matsuda, Y. Moritomo, *Jpn. J. Appl. Phys.* **2013**, *52*, 017301.

[70] A. C. Larson, R. B. Von Dreele, *Los Alamos Natl. Lab. Rep.* **2000**, *LAUR 86-748*.

[71] B. H. Toby, *J. Appl. Crystallogr.* **2001**, *34*, 210.